ISSN 1330-3651 (Print), ISSN 1848-6339 (Online) https://doi.org/10.17559/TV-20250312002462
Original scientific paper

Low-Dose X-Ray Visual Weld Defect Feature Extraction and Classification

Pengyu GAO, Yali HUANG, Jingguo SHE, Yangshuo TIAN, Xindu CHEN, Xiangdong GAO*

Abstract: This study proposes a low-dose X-ray-based nondestructive testing method for weld defect automatic detection, focusing on resistance spot welds and butt joint laser welds. By exploiting the high penetration capability and resolution of X-ray imaging, the proposed method detects internal defects such as porosity, cracks and lack of fusion through contrast analysis. Image preprocessing techniques including median filtering, Fourier and wavelet transforms, adaptive histogram equalization and Hough Transform were applied to suppress noises and enhance defect features. Also, Contrast Limited Adaptive Histogram Equalization effectively improves image contrast and reveals subtle defect patterns. For classification, the Random Forest algorithm was adopted to extract relevant features and perform defect recognition. Experimental results show that the proposed method achieves high accuracy in classifying weld defects, with strong generalization ability and minimal misclassification. The classification accuracy reached for resistance spot welds and laser welds confirms the method robustness. This approach enhances the automation and reliability of welding quality control by providing an efficient and accurate solution for internal defect identification. The contributions of this work lie in integrating advanced image processing with machine learning techniques for precise defect detection in complex weld structures using low-dose imaging, thus supporting intelligent inspection systems in industrial applications.

Keywords: feature extraction; non-destructive testing; random forest; weld defect detection; X-ray imaging

1 INTRODUCTION

X-ray imaging has become a crucial non-destructive testing (NDT) technique for detecting welding defects, particularly in manufacturing field such as aerospace, automotive, and construction, where weld integrity is vital. Increasingly stringent industry standards and varied service conditions have introduced complexity in defect morphology, making accurate detection more challenging [1, 2]. For example, surface defect inspection in automotive door seals still heavily depends on manual methods, which are inefficient and prone to human error [3]. With its high spatial resolution and deep penetration capability, X-ray imaging enables detailed inspection of internal weld structures without compromising component integrity. This is especially effective for identifying critical defects such as cracks, porosity, and incomplete penetration, which can severely weaken joints and cause structural failure. However, traditional X-ray systems are limited by high radiation exposure and operational complexity, which raise safety concerns and reduce efficiency, factors that hinder their broader industrial adoption [4-6].

To address these limitations, there is increasing interest in advanced X-ray non-destructive testing (NDT) techniques that reduce radiation exposure while improving detection speed and classification accuracy [7]. In comparison with conventional image processing, deep learning methods offer significant gains in both efficiency and accuracy, making them highly suitable for modern industrial applications [8]. In laser welding, advanced imaging techniques such as magneto-optical imaging have been successfully applied to detect and track weld positions with high precision [9]. A magneto-optical imaging method could also be applied to effectively detect the position of micro-weld joint under different welding conditions where welding path, weld gap or welding speed varies [10]. Studies on laser-arc hybrid welding further demonstrate that visual sensing technique including high-speed and X-ray imaging, can effectively monitor a keyhole dynamics and droplet behaviour, enabling real-time defect detection [11]. These developments reflect a clear shift towards low-dose, real-time imaging systems that offer improved safety and performance in weld defect inspection.

This study presents a novel low-dose X-ray NDT method aimed at improving weld quality assessment while reducing radiation risks. The approach combines Random Forest classifiers with feature recognition algorithms to enhance the accuracy of defect classification in X-ray weld images. By establishing an efficient recognition and classification system, the method supports the development of automation and intelligent decision-making in welding processes. The proposed framework provides a solid technical basis for the future implementation of automated weld inspection in industrial settings, thereby advancing weld defect detection technologies.

2 X-RAY IMAGE DETECTION OF WELD DEFECTS

2.1 Challenges of Detecting Weld Defects

Non-destructive testing (NDT) plays a vital role in ensuring the quality and reliability of welded joints, with X-ray inspection being one of the most widely used techniques. Its superior penetration capability allows for detailed internal imaging without damaging components, making it essential for detecting common defects such as cracks, porosity, and lack of fusion [12]. Advances in deep learning have demonstrated remarkable performance in weld defect detection, often surpassing manual inspection. However, these methods typically require large labelled datasets and significant computational resources, limiting their industrial applicability [13]. Traditional machine learning methods have also shown effectiveness, particularly by utilising automatically collected process data for defect prediction, although there still exist techniques for improvement in real-time processing, computational efficiency, and adaptability to complex industrial environments [14].

Despite these advances of NDT, real-time X-ray defect detection in complicated welding remains challenging. This study proposes a low-dose X-ray NDT framework that combines preprocessing techniques, including CLAHE, GLCM analysis, and Hamming distance, with a Random

Forest classifier to enhance classification accuracy while reducing radiation exposure. Unlike conventional methods, the approach leverages the robustness of Random Forest in handling noisy, complex data, offering a scalable and data-efficient alternative to deep learning. Future work will aim to improve model robustness and adaptability for practical industrial deployment.

2.2 Application of Random Forest in X-Ray Image Detection

Random Forest has demonstrated strong performance in X-ray image analysis for defect recognition and classification tasks [15]. For instance, in detecting assembly defects in thermal battery monomers, it has been used to classify defect types based on features such as texture and contrast. Its ensemble structure, comprising multiple decision trees, enhances classification accuracy and robustness, particularly in complex and noisy datasets [16]. Additionally, random feature selection and sampling during training help mitigate overfitting, offering high adaptability, especially for imbalanced datasets. Random Forest has also shown reliable results in fields such as welding defect detection and medical imaging, improving both accuracy and efficiency in automated inspection systems.

In comparison with deep learning approaches such as Convolutional Neural Networks (CNNs) and Transformer-based architectures, Random Forest exhibits notable advantages in terms of computational efficiency and practical applicability. While CNNs and Transformers typically require large volumes of labelled data and considerable computational resources, Random Forest performs reliably with smaller datasets and lower hardware demands, making it well-suited to industrial environments with limited data availability and restricted computing capabilities. Furthermore, in contrast to deep learning models often regarded as black-box systems, Random Forest provides interpretable outputs by quantifying feature importance, thereby facilitating greater transparency and ease of integration in real-world industrial applications [17].

3 IMAGE PROCESSING AND FEATURE EXTRACTION

3.1 Image Preprocessing and Enhancement

Image preprocessing plays a pivotal role in X-ray-based defect detection, aiming to enhance image clarity, suppress noises, and emphasise features associated with welding defects. In this study, a combination of median filtering and Fourier transform filtering is employed for resistance spot weld X-ray images, whereas laser weld images are processed using median filtering alongside wavelet transform filtering. These techniques have demonstrated significant effectiveness in reducing image noises and improving the visual detectability of defects. As depicted in Fig. 1, the impact of the denoising algorithms on image quality enhancement is clearly observable. Fig. 1a displays an original resistance spot weld image, while Fig. 1b presents the corresponding raw X-ray image. Fig. 1c illustrates the substantial improvement in visual quality following the application of the proposed preprocessing techniques. Median filtering successfully attenuates random noises, whereas Fourier transform filtering further refines an image by accentuating edge features, resulting in sharper weld contours and improved defect visibility.

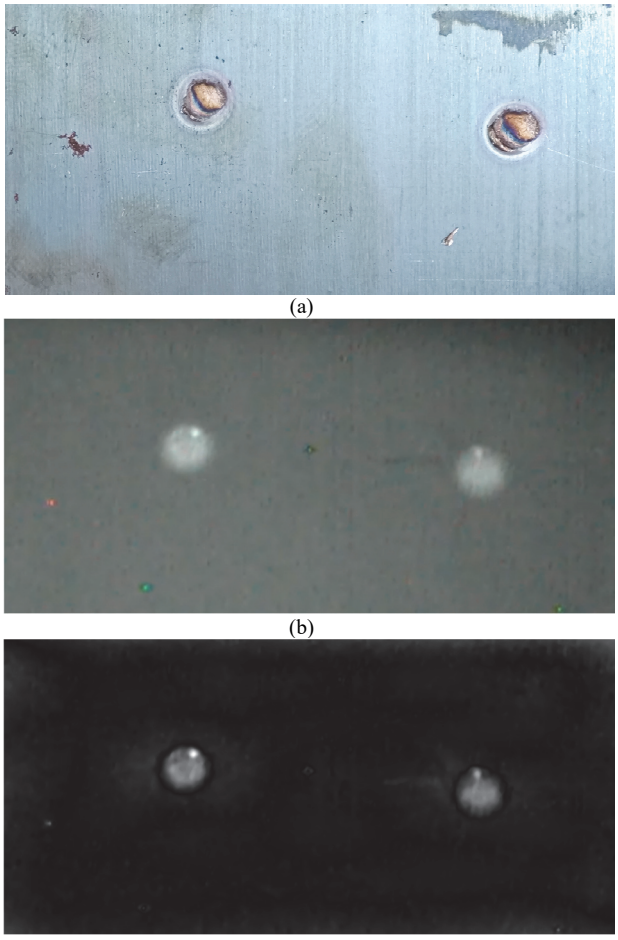

(a)

(b)

(c)

Figure 1 Image processing of resistance welding spots
(a) original image (b) X-ray image (c) image after median and Fourier filtering

Median filtering is effective in suppressing Gaussian noise while preserving essential edge information, which is vital for accurate weld feature extraction and defect recognition. Fourier and wavelet transform-based filtering techniques further enhance local image characteristics, thereby improving the visibility of defects. Fig. 2 illustrates the results of denoising a laser weld X-ray image using a combined approach involving median filtering and wavelet transform filtering. Fig. 2a presents the original X-ray image of the laser weld, whereas Fig. 2b shows the processed image obtained after applying the integrated filtering method. Experimental results clearly demonstrate that this technique effectively removes noises while retaining critical image features, particularly the edge details of the weld seam. These enhanced images form a high-quality basis for subsequent image analysis and defect detection procedures.

The Contrast Limited Adaptive Histogram Equalisation (CLAHE) algorithm enhances boundary details, equalises brightness distribution, and accentuates fine image features, thereby increasing the contrast in weld seams or weld spots. As illustrated in Fig. 3 and Fig. 4, corresponding to the post-denoising samples shown in Fig. 1c and Fig. 2b respectively, CLAHE is demonstrated to be

an effective method for adaptive histogram equalisation following noise reduction, leading to improved boundary sharpness and overall image contrast.

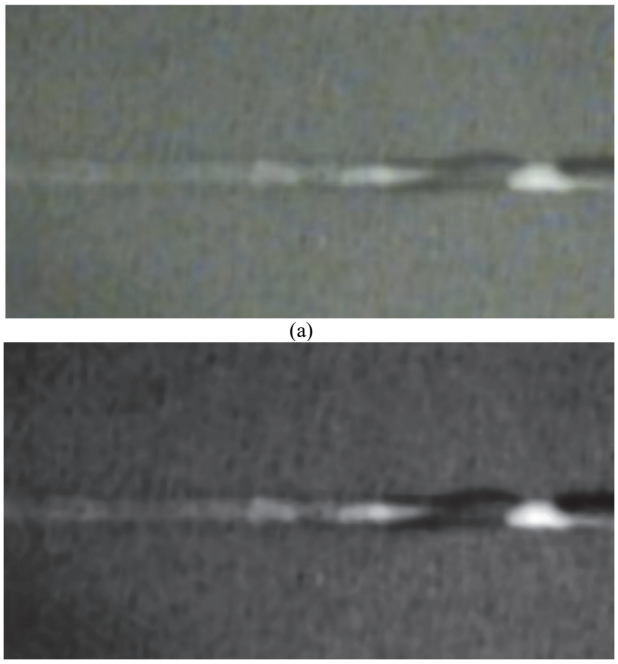

(a) (b)

Figure 2 Image processing of laser welding seam
(a) original X-ray image (b) image after median and wavelet transform filtering

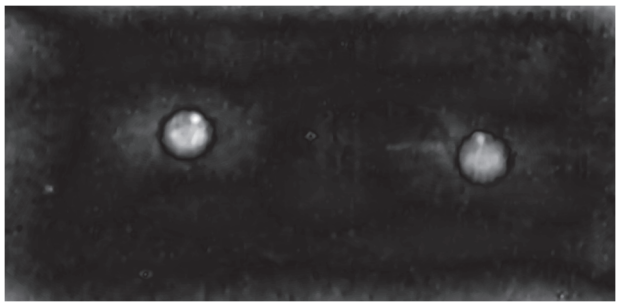

Figure 3 Enhancement of spot welding X-ray images through filtering

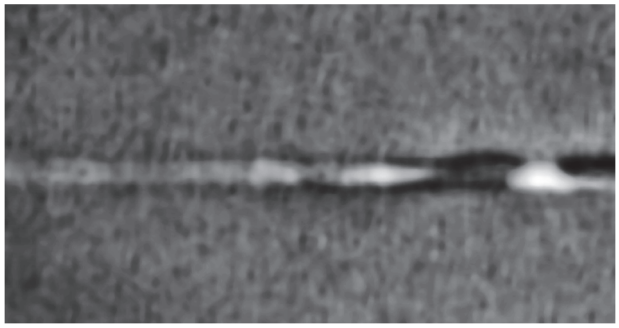

Figure 4 Filtering and enhancement of laser welding X-ray images

3.2 ROI Extraction

The Hough Transform is a well-established feature extraction technique commonly employed for detecting specific geometric shapes, such as circles, within images. It is particularly effective for identifying circular weld points in resistance spot welding. By mapping the image space into a parameter space and identifying local maxima, this method facilitates the rapid localisation of circular coordinates, thereby enabling efficient extraction of regions of interest (ROI).

As illustrated in Fig. 5, which corresponds to the sample shown in Fig. 1c, two ROIs were extracted from a spot welding X-ray image using rectangular cropping following the application of the Hough Transform. However, conventional linear methods often encounter limitations when dealing with complex and highly variable weld features. To address this challenge, a thresholding technique was employed to enhance contrast and improve the visibility of the weld area in the binarized image. Subsequently, contour detection was used to identify prominent features, and the bounding box of the largest contour was calculated to enable accurate extraction of the weld region.

Furthermore, image slicing based on grey-level region coordinates was implemented to extract multiple ROIs for detailed feature analysis. Fig. 6, corresponding to Fig. 2b, presents representative weld region samples obtained using this approach.

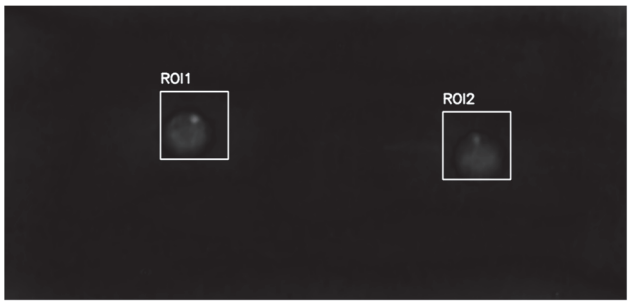

Figure 5 ROI from spot welding X-ray image

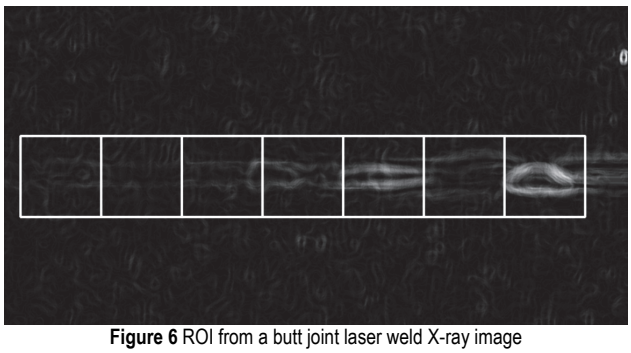

Figure 6 ROI from a butt joint laser weld X-ray image

3.3 Feature Vector Extraction

The Gray Level Co-occurrence Matrix (GLCM) was employed to extract key statistical texture features, Energy, Entropy, Contrast, Correlation, and Inverse Difference Moment (IDM), from resistance spot welding X-ray images for defect characterisation. The GLCM is defined as [18]:

$$P\left(i,j\middle|a,\,b,\,\theta\right)=\begin{cases}\left(x,y\right)\middle|f\left(x,y\right)=i,\\ f\left(x+a,y+b\right)=j\end{cases} \tag{1}$$

where the matrix element $P(i, j \mid a, b, \theta)$ represents the frequency at which a pixel with intensity i co-occurs with a neighbouring pixel of intensity j at an offset (a, b) in a specified direction θ. Here, (x, y) denotes the pixel coordinates, and $f(x, y)$ represents the intensity value at that

position. The variables a and b define the horizontal and vertical displacements between pixel pairs, while θ determines the directional angle for computation. The formula iterates over all image pixels, where $x, y = 0, 1, 2, \ldots, (L-1)$, with L typically representing the number of image gray levels.

1. Energy, a measure of texture uniformity, is calculated as the sum of the squared elements in the GLCM:

$$\text{Energy} = \sum_{i=0}^{N-1}\sum_{j=0}^{N-1}\left[P(i,j)\right]^2 \tag{2}$$

where i and j represent pixel gray levels, ranging from 0 to $L-1$ and $P(i, j)$ denotes the frequency of pixel pairs with gray levels i and j in the GLCM. L is the number of gray levels in the image.

2. Entropy, which quantifies the randomness or complexity of the texture, is given by:

$$\text{Entropy} = -\sum_{i=0}^{N-1}\sum_{j=0}^{N-1}\left(P(i,j)\log P(i,j)\right) \tag{3}$$

3. Contrast, which evaluates the intensity contrast between a pixel and its neighbour over the entire image, is expressed as:

$$\text{Contrast} = \sum_{i=0}^{N-1}\sum_{j=0}^{N-1}P(i,j)(i-j)^2 \tag{4}$$

4. Correlation, which indicates the degree of linear dependency between the grey levels of pixel pairs, is calculated as:

$$\text{Correlation} = \sum_{i=0}^{N-1}\sum_{j=0}^{N-1}\frac{(ij)P(i,j)-\mu_i\mu_j}{\sigma_i\sigma_j} \tag{5}$$

where μ_i and μ_j are the means of rows and columns in the GLCM, and σ_i and σ_j are their respective standard deviations.

5. Inverse Difference Moment (IDM), a metric indicating texture smoothness and local homogeneity, is defined as:

$$\text{IDM} = \sum_{i=0}^{N-1}\sum_{j=0}^{N-1}\frac{P(i,j)}{1+(i+j)^2} \tag{6}$$

Tab. 1 presents the extracted GLCM feature values corresponding to the ROI1 image illustrated in Fig. 5, demonstrating how these statistical descriptors can assist in the characterisation of welding defects such as cracks, porosity, and lack of fusion. By analysing these feature values, a more profound understanding of the texture patterns associated with each defect type is attained.

Table 1 Features of spot welding crack legends in GLCM

ROI	Energy	Entropy	Contrast	Correlation
ROI1	0.14	7.09	1.69	1.00

Based on the statistical analysis of 2000-dimensional feature vectors extracted from X-ray images of resistance spot welds, a total of 500 samples were collected for each category: defect-free, porosity, cracks, and lack of fusion. As illustrated in Fig. 7, the extracted features were organised into segments: dimensions 1-500 correspond to Energy, 501-1000 to Entropy, 1001-1500 to Contrast, 1501-2000 to Correlation, and 2001-2500 to Inverse Difference Moment (IDM). The vertical axis indicates the feature values across different defect categories. Fig. 7a to Fig. 7d represent the distributions for defect-free, cracks, porosity, and lack of fusion, respectively.

Distinct variations are observed in the feature distributions across defect types, particularly in the Entropy and Contrast components. While Energy, Correlation, and IDM display relatively uniform distributions among the categories, the Entropy values for defect-free, porosity, and lack of fusion samples are closely aligned and differ markedly from those associated with crack defects. In terms of Contrast, porosity exhibits a broader spread and higher feature values in comparison with other categories, whereas cracks present the lowest and most concentrated values, albeit with occasional outliers. These findings suggest that texture features derived from the GLCM, especially Entropy and Contrast, have significant potential for distinguishing among various weld defect types.

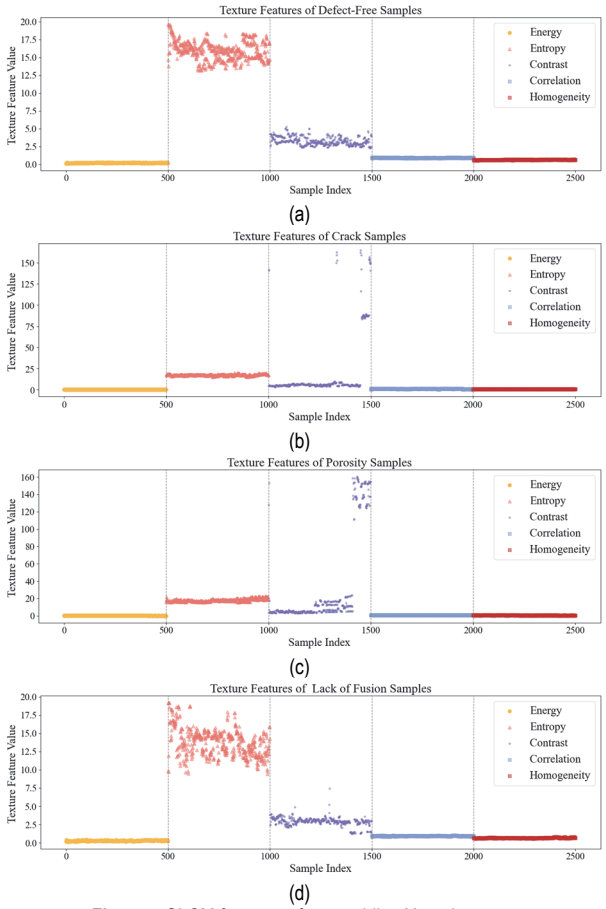

Figure 7 GLCM features of spotwelding X-ray images
(a) defect-free (b) crack (c) porosity (d) lack of fusion

The dispersed spatial distribution of laser welds in X-ray images presents substantial challenges for accurate segmentation, rendering it difficult to effectively isolate

the weld region from the surrounding background. Conventional texture analysis approaches, such as those based on the Grey Level Co-occurrence Matrix (GLCM), including Energy, Entropy, Contrast, Correlation, and Homogeneity, often fail to satisfy the real-time processing demands required by laser weld video streams.

To overcome these limitations, a feature extraction method based on the Hamming distance is introduced as a more computationally efficient solution. By comparing binary descriptors of key points, the Hamming distance facilitates the identification of various welding defects, such as porosity, cracks, and lack of fusion. This approach not only improves the accuracy of defect recognition but also supports real-time implementation, making it particularly suitable for industrial applications. The Hamming distance is calculated as follows:

$$\tau(C; r, s) = \begin{cases} 0, & \text{if } T(C, r) = T(C, s) \\ 1, & \text{if } T(C, r) \neq T(C, s) \end{cases} \tag{7}$$

where C represents the image or feature point being analyzed, r and s are the indices or positions of the feature points being compared, $T(C, r)$ and $T(C, s)$ are the descriptors or feature values of the r-th and s-th feature points of image C, respectively.

The final feature point descriptor is expressed as:

$$f(C) = \sum_{t=1}^{k} 2^{t-1} \cdot \tau(C; r, s) \tag{8}$$

where $f(C)$ is the final feature descriptor for the image C, k is the total number of feature points or the dimensionality of the feature descriptor, $\tau(C; r, s)$ is the Hamming distance calculated between the feature points r and s, t is the index used for summing over the feature points, representing the t-th feature point in the descriptor. These formulas for computing Hamming distance and feature point descriptors are adapted from standard image processing methods described in [18].

To assess the effectiveness of the proposed feature extraction method, a set of 20 welding X-ray images of the same category was selected for feature matching and Hamming distance analysis. The results are presented in Tab. 2. A smaller Hamming distance observed between defect-free images indicates a higher degree of similarity, whereas the larger Hamming distances associated with lack of fusion images reflect greater intra-class variability for this particular defect type.

Table 2 Hamming distance of various X-ray images of laser welding bead

Types	No defect	Porosity	Sag	Lack of fusion
average	60.38	73.52	79.60	85.32

In addition, this study integrates five grayscale distribution features, mean, variance, energy, entropy, and contrast, to enhance the discriminative capability of the extracted feature vectors. The grayscale mean and variance are computed using standard image analysis methods, as described in [19], and are defined as follows:

$$M = \sum_{k=1}^{m} \sum_{l=1}^{n} T(k, l) \tag{9}$$

where Mean (M) represents the average gray value of all pixels in an image, indicating the overall brightness level. A higher mean value suggests that the image tends to be brighter or whiter. In the formula, $T(k, l)$ represents the gray value of the pixel at position (k, l), while k and l are the row and column indices, respectively. The dimensions of the image are given by m (number of rows) and n (number of columns). The mean is calculated by summing all pixel values across the entire image.

$$V^2 = \sum_{k=1}^{m} \sum_{l=1}^{n} \left(T(k, l) - M\right)^2 \tag{10}$$

where Variance (V^2) measures the degree of dispersion in pixel gray values, reflecting the complexity of the image texture. A larger variance indicates a more uneven distribution of pixel intensities and a more complex texture. In this formula, M is the mean gray value, and the variance is computed as the sum of the squared differences between each pixel's gray value and the mean. A higher variance suggests greater texture variation and more significant contrast in the image.

A statistical analysis was performed on 2000-dimensional feature vectors extracted from X-ray images of laser weld seams, with 500 samples selected for each defect category: defect-free, porosity, pits, and lack of fusion. As illustrated in Fig. 8, the horizontal axis represents segmented feature dimensions based on metric type: dimensions 1-500 correspond to Hamming distance, 501-1000 to grey-level mean, 10011500 to grey-level variance, 1501-2000 to grey-level energy, 2001-2500 to grey-level entropy, and 2501-3000 to grey-level contrast. The vertical axis displays the feature values associated with the respective defect categories.

Fig. 8a shows the feature distribution for defect-free samples. The first four segments (dimensions 1-2000) exhibit relatively low and stable values, indicating a high degree of similarity in texture features among the samples. A notable increase in grey-level contrast is observed in the final segment (2501-3000), reflecting greater variability in texture characteristics. Fig. 8b presents the distribution for porosity samples, which also demonstrates an increase in contrast values in the final segment, although less pronounced than in the defect-free category, suggesting moderate texture variation. Fig. 8c depicts pit samples, where the contrast values in the final segment increase more than those for porosity, but remain lower than those of defect-free samples. In contrast, Fig. 8d illustrates the distribution for lack of fusion samples, where the increase in grey-level contrast within the last feature segment is the most prominent among all categories, indicating substantial intra-class texture variation.

These findings suggest that the selected combination of statistical and texture-based features, particularly grey-level contrast, exhibits strong potential for discriminating between different types of weld defects.

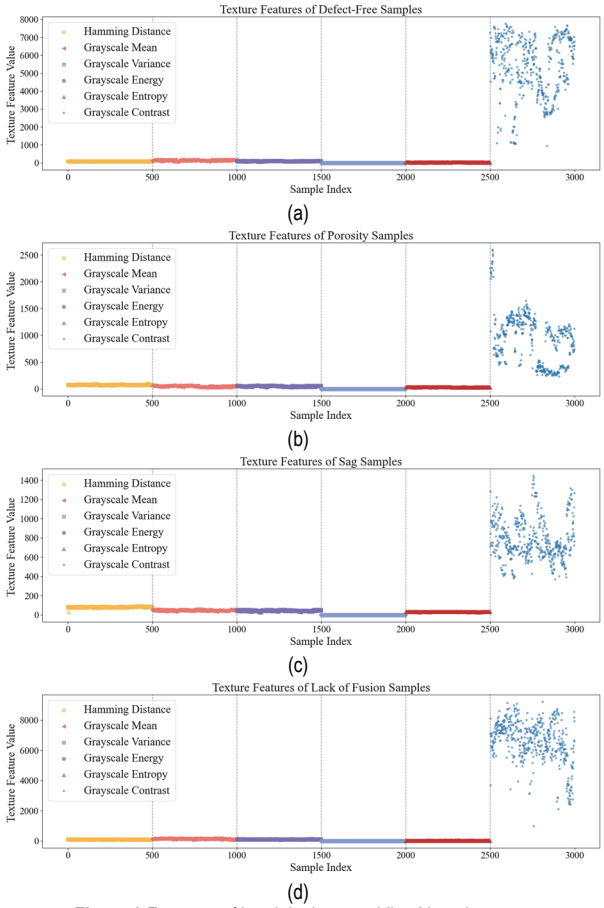

Figure 8 Features of butt joint laser welding X-ray images (a) defect-free (b) porosity (c) sag (d) lack of fusion

4 WELD DEFECT CLASSIFICATION METHODS

4.1 Random Forest Classification Process

Random Forest is an ensemble learning algorithm that constructs multiple decision trees using randomly selected subsets of data and features, with final predictions made through majority voting. In this study, Random Forest was adopted as the primary classifier for detecting welding defects in both resistance spot welding and laser welding applications.

This choice was informed by a comprehensive comparative analysis. Although XGBoost and a shallow neural network achieved marginally higher accuracies (92.33% and 92.17%, respectively), Random Forest delivered comparable performance, achieving an accuracy of 91.67% and a macro F1-score of 0.92, while offering enhanced interpretability, reduced computational complexity, and greater robustness with minimal hyperparameter tuning. In contrast, the support vector machine (SVM) underperformed, with an accuracy of only 79.33%. The classification procedure was structured as follows:

1. Data Preparation: Feature vectors were extracted from images across four defect categories.

2. Feature Selection: Six features, Hamming distance, mean, standard deviation, energy, entropy, and contrast, were used based on domain knowledge and experimental validation.

3. Model Training: For the resistance spot welding task, the training dataset comprised 2000 images, equally distributed across the four defect classes (500 images per class). A five-fold cross-validation approach was implemented, with each fold containing 400 images. The optimised Random Forest model utilised 100 decision trees, each constrained to a maximum depth of 10. To mitigate overfitting while preserving model complexity, the minimum number of samples required to split an internal node was set to 2, with at least 2 samples per leaf node. A square root proportion of the total feature set was considered at each split.

For the laser welding task, the training set included 1600 images, with a slight class imbalance. Stratified five-fold cross-validation was applied to maintain class distribution across folds. The final model incorporated 150 trees with a maximum depth of 10. The splitting criterion required a minimum of 2 samples for node division and at least 1 sample per leaf node, with a square root of the total number of features evaluated at each split.

4. Model Evaluation: An independent test set was reserved for final evaluation. For resistance spot welding, the test set comprised 1200 images (300 per class), while for laser welding, it consisted of 400 images with proportions consistent with the training distribution. Final performance metrics were computed based on this independent evaluation.

4.2 Classification Results For Resistance Welding

The classification performance of the optimised model was evaluated using a balanced test set comprising 1200 samples, evenly distributed across four classes: Crack, Lack of Fusion, Defect-Free, and Porosity. The model achieved an overall accuracy of 93.0%, demonstrating strong generalisation following hyperparameter optimisation. Detailed classification metrics are summarized in Tab. 3. The model exhibited consistently high precision, recall, and F1-scores across all categories. The Lack of Fusion class yielded the best results, with all three metrics, precision, recall, and F1-score, reaching 0.97. The Crack and Defect-Free classes achieved F1-scores of approximately 0.92, while the Porosity class reported slightly lower values, with an F1-score of 0.89.

The confusion matrix, illustrated in Fig. 9a, reveals the primary misclassification trends. Specifically, 24 Crack samples were misclassified as Porosity, likely due to overlapping texture characteristics such as contrast and entropy. Lack of Fusion samples were occasionally confused with the Crack and Defect-Free classes. Moreover, certain Defect-Free samples exhibited partial feature similarity with defective categories, leading to classification errors. Porosity samples were also frequently misclassified as Crack or Defect-Free.

Feature importance analysis (Fig. 9b) highlights contrast, correlation, and entropy as the most influential features contributing to classification performance. The similarity of these features across particular classes may account for some of the observed classification ambiguities.

Learning curves presented in Fig. 9c confirm the model robustness. While training accuracy remained consistently above 98% across increasing training set sizes, validation accuracy improved significantly, from approximately 25% at small sample sizes to 92.95% at the largest training size (1600 samples). This trend indicates

reduced overfitting and improved generalisation with the expansion of training data.

Table 3 The random forest classification results for resistance welding

Class	Precision	Recall	F1-Score	Support
Crack	0.91	0.92	0.92	300
Lack of fusion	0.97	0.97	0.97	300
Defect-Free	0.93	0.92	0.92	300
Porosity	0.89	0.90	0.89	300
Accuracy			0.93	1200
Macro Avg	0.93	0.93	0.93	1200
Weighted Avg	0.93	0.93	0.93	1200

It has been shown that the optimised model delivers robust and well-balanced classification performance across all defect categories. Residual misclassifications are primarily attributed to intrinsic feature similarities between specific weld defect types. Future work should explore advanced feature extraction techniques or alternative classification architectures to further enhance the model discriminative capability.

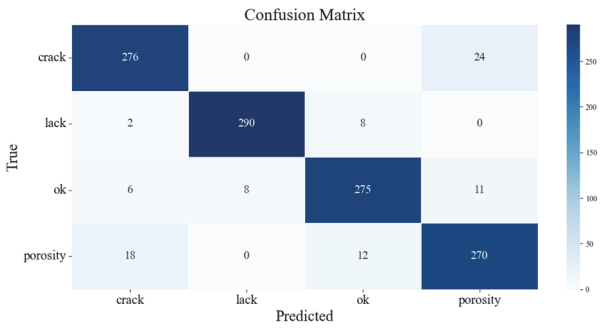

(a)

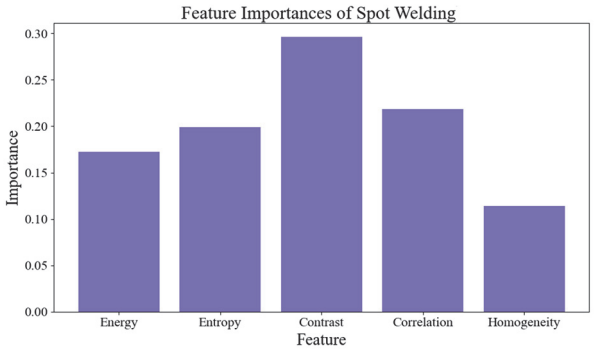

(b)

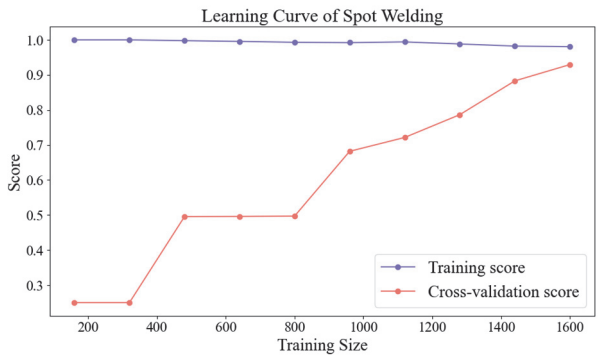

(c)

Figure 9 The random forest classification results for resistance spot welding (a) confusion matrix (b) feature importance (c) learning curve

4.3 Classification Results for Laser Welding

To evaluate the performance of the proposed Random Forest classifier in laser welding defect classification, a comprehensive set of experiments was conducted using a test dataset comprising 400 samples distributed across four categories: Sag, Porosity, Defect-Free, and Lack of Fusion. The classification results are summarised in Tab. 4, where the model achieved an overall test accuracy of 91.25%, indicating strong discriminative capability under varying welding conditions.

As shown in Tab. 4, the model attained high precision and recall scores across all defect categories. The highest F1-score was achieved for the Sag class (0.93), while the Defect-Free class yielded a slightly lower F1-score of 0.88, potentially due to feature similarities with minor defect types.

The confusion matrix presented in Fig. 10a illustrates the principal misclassification patterns. Specifically, 10 Porosity samples were misclassified as Sag, and 4 Sag samples were classified as Porosity, likely due to overlapping textural characteristics, particularly in contrast and entropy. In addition, 10 Defect-Free samples were misclassified as Lack of Fusion, and 3 Lack of Fusion samples were incorrectly labelled as Defect-Free, indicating partial feature overlap between fusion-deficient welds and non-defective welds.

Feature importance analysis, shown in Fig. 10b, identifies Standard Deviation, Mean, and Contrast as the most influential features driving the model's predictions. These features effectively represent the statistical and textural properties of the weld surface. Secondary features, including Hamming Distance, Energy, and Entropy, also contributed meaningfully, particularly in ambiguous cases where more nuanced discrimination was required.

To assess the model generalisation capability, a learning curve was constructed using training set sizes ranging from 128 to 1,280 samples, as illustrated in Fig. 10c. The training accuracy exhibited a slight decline from 100% to 99.05%, while validation accuracy improved significantly from 84.88% to 92.38%, indicating convergence between training and validation performance. This suggests that increasing the size of the training set effectively mitigated overfitting and improved generalisation.

The Random Forest classifier demonstrated robust and well-balanced performance across all evaluated categories, including both Defect-Free and defective weld types. The close alignment between cross-validation and test accuracy, alongside the interpretability of feature contributions, confirms the model reliability and suitability for practical industrial applications.

Table 4 The random forest classification results forlaser welding

Class	Precision	Recall	F1-Score	Support
Sag	0.91	0.96	0.93	104
Porosity	0.94	0.89	0.92	95
Defect-free	0.89	0.88	0.88	88
Lack of fusion	0.91	0.91	0.91	113
Accuracy	-	-	0.91	400
Macro Avg	0.91	0.91	0.91	400
Weighted Avg	0.91	0.91	0.91	400

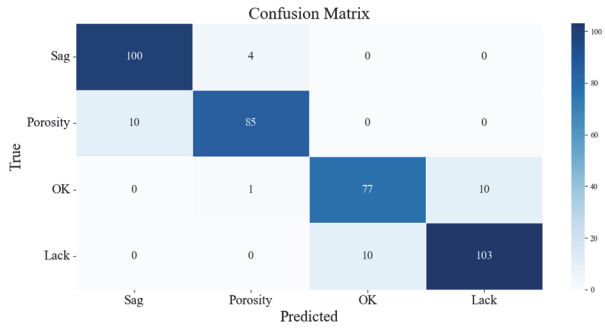

(a)

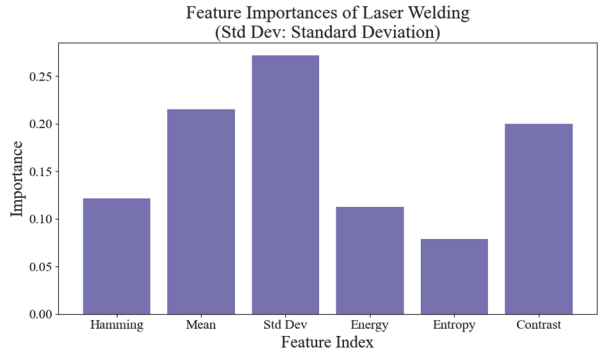

(b)

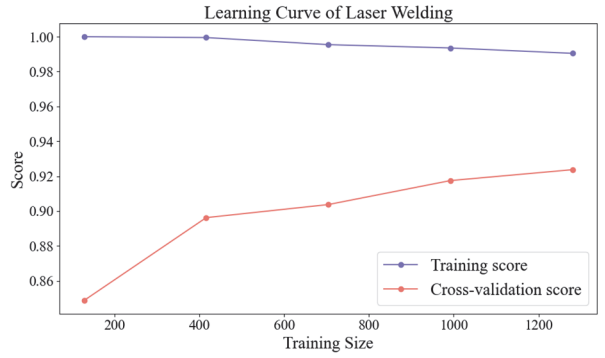

(c)

Figure 10 The random forest classification results for laser welding (a) confusion matrix (b) feature importance (c) learning curve

5 CONCLUSIONS

This study presents a low-dose X-ray imaging approach for non-destructive testing (NDT) of welding defects in both resistance spot welding and laser welding. By leveraging recent advances in detector sensitivity and image processing algorithms, the proposed method enhances inspection speed and classification accuracy, thereby fulfilling the requirements of automated welding quality assurance.

To reduce noises and emphasise weld defect features, a series of preprocessing techniques, including median filtering, Fourier transform, and wavelet transform, was applied. Texture features were extracted using the Grey Level Co-occurrence Matrix (GLCM), with contrast identified as the most discriminative parameter for characterising defect types. A Random Forest classifier, optimised through a randomised hyperparameter search strategy, achieved classification accuracies of 93.00% for resistance spot welding and 91.25% for laser welding, respectively.

In addition to high classification accuracy, the proposed method demonstrates excellent computational efficiency. The total training time, including hyperparameter optimisation, was less than 80 seconds. Inference time per sample was below 0.04 milliseconds, thereby satisfying real-time constraints such as 30 frames per second (FPS). Peak memory consumption remained below 300 MB, confirming the feasibility of deploying the method on resource-limited platforms, including industrial PCs and embedded edge devices. These results affirm not only the effectiveness but also the real-time applicability of the proposed approach, supporting its integration into automated welding defect inspection systems.

Acknowledgements

This work is supported by the Guangdong Provincial Natural Science Foundation of China under Grant 2023A1515012172, and the Guangzhou Municipal Special Fund Project for Scientific and Technological Innovation and Development under Grant 2023B03J1326.

6 REFERENCES

[1] Silva, M. I., Malitckii, E., Santos, T. G., & Vilaça, P. (2023). Review of conventional and advanced non-destructive testing techniques for detection and characterization of small-scale defects. *Progress in Materials Science*, *138*, 101155. https://doi.org/10.1016/j.pmatsci.2023.101155

[2] Tyystjärvi, T., Fridolf, P., Rosell, A., & Virkkunen, I. (2024). Deploying machine learning for radiography of aerospace welds. *Journal of Nondestructive Evaluation*, *43*(1), 24. https://doi.org/10.1007/s10921-023-01041-w

[3 Lv, B., Gao, X., Feng, S., & Yuan, J. (2022). Deep learning detection algorithm for surface defects of automobile door seals. *Tehnički vjesnik*, *29*(5), 1499-1506. https://doi.org/10.17559/TV-20211219032823

[4] Liu, T., Zheng, P., Bao, J., & Chen, H. (2023). A state-of-the-art survey of welding radiographic image analysis: Challenges, technologies and applications. *Measurement*, *214*, 112821. https://doi.org/10.1016/j.measurement.2023.112821

[5] Zhang, R., Liu, D., Bai, Q., Fu, L., Hu, J., & Song, J. (2024). Research on X-ray weld seam defect detection and size measurement method based on neural network self-optimization. *Engineering Applications of Artificial Intelligence*, *133*, 108045. https://doi.org/10.1016/j.engappai.2024.108045

[6] Vasan, V., Sridharan, N. V., Balasundaram, R. J., & Vaithiyanathan, S. (2024). Ensemble-based deep learning model for welding defect detection and classification. *Engineering Applications of Artificial Intelligence*, *136*, 108961. https://doi.org/10.1016/j.engappai.2024.108961

[7] Ajmi, C., Zapata, J., Elferchichi, S., & Laabidi, K. (2024). Advanced Faster-RCNN model for automated recognition and detection of weld defects on a limited X-ray image dataset. *Journal of Nondestructive Evaluation*, *43*(1), 14. https://doi.org/10.1007/s10921-023-01032-x

[8] Archana, R. & Jeevaraj, P. S. E. (2024). Deep learning models for digital image processing: A review. *Artificial Intelligence Review*, *57*(1), 11. https://doi.org/10.1007/s10462-023-10631-z

[9] Gao, X., Mo, L., You, D., & Li, Z. (2017). Tight butt joint weld detection based on optical flow and particle filtering of magneto-optical imaging. *Mechanical Systems and Signal Processing*, *96*, 16-30. https://doi.org/10.1016/j.ymssp.2017.04.001

[10] Gao, X., Liu, Y., & You, D. (2014). Detection of micro-weld joint by magneto-optical imaging. *Optic sand Laser Technology*, *32*, 141-151. https://doi.org/10.1016/j.optlastec.2013.12.027
[11] Fan, X., Gao, X., Zhang, N., Ye, G., Liu, G., & Zhang, Y. (2022). Monitoring of 304 austenitic stainless-steel laser-MIG hybrid welding process based on EMD-SVM. *Journal of Manufacturing Processes*, *73*, 736-747. https://doi.org/10.1016/j.jmapro.2021.11.031
[12] Wang, P., Li, L., Li, X., Duan, L., Lü, Z., & Di, R. (2025). An automatic welding defect detection method based on deep learning for super 8-bit high grayscale X-ray films of solid rocket motor shells. *NDT & E International*, *151*, 103306. https://doi.org/10.1016/j.ndteint.2024.103306
[13] Szőlősi, J., Szekeres, B. J., Magyar, P., Adrián, B., Farkas, G., & Andó, M. (2024). Welding defect detection with image processing on a custom small dataset: A comparative study. *IET Collaborative Intelligent Manufacturing*, *6*(4), e70005. https://doi.org/10.1049/cim2.70005
[14] Ciravegna, G., Galante, F., Giordano, D., Cerquitelli, T., & Mellia, M. (2024). Fault Prediction in Resistance Spot Welding: A Comparison of Machine Learning Approaches. *Electronics*, *13*(18), 3693. https://doi.org/10.3390/electronics13183693
[15] Ramana, E. V., Penekalapati, S. V., & Namala, K. K. (2024). Identification of weld sub-surface defects by radiographic images using texture features. *E3S Web of Conferences*, *552*, 01017. https://doi.org/10.1051/e3sconf/202455201017
[16] Say, D., Zidi, S., Qaisar, S. M., & Krichen, M. (2023). Automated categorization of multiclass welding defects using the x-ray image augmentation and convolutional neural network. *Sensors*, *23*(14), 6422. https://doi.org/10.3390/s23146422
[17] Block, S. B., Da Silva, R. D., Lazzaretti, A. E., & Minetto, R. (2024). LoHi-WELD: A novel industrial dataset for weld defect detection and classification, a deep learning study, and future perspectives. *IEEE Access*. https://doi.org/10.1109/ACCESS.2024.3407019
[18] Zubair, A. & Alo, O. (2019). Grey Level Co-occurrence Matrix (GLCM) based second order statistics for image texture analysis. *International Journal of Science and Engineering Investigations*, *8*(93), 64-73.
[19] Sluijterman, L., Cator, E., & Heskes, T. (2024). Optimal training of mean variance estimation neural networks. *Neurocomputing*, *597*, 127929. https://doi.org/10.1016/j.neucom.2024.127929

Contact information:

Pengyu GAO, Doctoral Student
Guangdong provincial Welding Engineering Technology Research Center,
Guangdong University of Technology,
Guangzhou 510006, Guangdong, China
E-mail: perrypgao@gmail.com

Yali HUANG, Postgraduate Student
Guangdong provincial Welding Engineering Technology Research Center,
Guangdong University of Technology,
Guangzhou 510006, Guangdong, China
E-mail: 1677694175@qq.com

Jingguo SHE, Postgraduate Student
Guangdong provincial Welding Engineering Technology Research Center,
Guangdong University of Technology,
Guangzhou 510006, Guangdong, China
E-mail: 1280170438@qq.com

Yangshuo TIAN, Postgraduate Student
Guangdong provincial Welding Engineering Technology Research Center,
Guangdong University of Technology,
Guangzhou 510006, Guangdong, China
E-mail: 982551164@qq.com

Xindu CHEN, Professor
School of Electromechanical Engineering,
Guangdong University of Technology,
Guangzhou 510006, Guangdong, China
E-mail: chenxindu@gdut.edu.cn

Xiangdong GAO, Professor
(Corresponding author)
1) Guangdong provincial Welding Engineering Technology Research Center,
Guangdong University of Technology,
Guangzhou 510006, Guangdong, China
2) Guangzhou Zhengtian Technology Co., Ltd,
Guangzhou 510006, China
E-mail: gaoxd@gdut.edu.cn